Comparing Frequency Transfer via GNSS and Fiber in a Common-clock Configuration

Ahmed Elmaghraby, Thomas Krawinkel, Steffen Schön,
Leibniz University Hannover, Institut für Erdmessung, Schneiderberg 50, 30167 Hannover, Germany
Ann-Kathrin Kniggendorf, Alexander Kuhl, Shambo Mukherjee, Jochen Kronjäger, Dirk Piester,
Physikalisch-Technische Bundesanstalt, Bundesallee 100, 38116 Braunschweig, Germany

Abstract

Realizing a clock-based geodetic network with a relative uncertainty level of 10^{-18} has been a significant objective for the scientific community. This network can be utilized for realizing more accurate geodetic reference frames and for testing the fundamental laws of physics, such as the theory of relativity. Typically, optical fibers are connecting optical clocks in such a network. For the last decades, Global Navigation Satellite Systems (GNSSs) have built a trustful and easy-setup method for frequency and time transfer. However, recently optical fiber link networks showed better frequency instability. In this study, we investigate the limits of GNSS-based frequency transfer links with the help of an optical fiber link as ground truth. Therefore, we analyze the GNSS data acquired in a dedicated common-clock experiment over a 52 km baseline. We focus on developing two algorithms to estimate the receiver clock differences, hence the frequency instability. These are the single difference (SD) approach with ambiguity fixing as a common view technique, and precise point positioning as an all in-view technique. We discuss the frequency instability achieved by the optical fiber link as well. We evaluate further the performance by computing the modified Allan deviation for both cases. The results show that the ambiguity-fixed solution of SD-CV improves the relative frequency instability via GNSS to reach the order of $3\text{–}5 \cdot 10^{-17}$ at one day averaging time. In the optical fiber link, which is the basis of the common clock setup, the round-trip instability shows better performance for all averaging times.

I. Introduction

Global Navigation Satellite Systems (GNSSs) have been an essential part of frequency dissemination, UTC traceability and comparison systems at many national metrological institutes (Defraigne, 2017; Bauch et al., 2020; Defraigne et al., 2022; Defraigne et al., 2023; Piester et al., 2024). The realized frequency instability is not yet fulfilling the requirements for all geodetic applications. For example, a unified height system based on chronometric leveling with state-of-the-art optical clocks requires relative uncertainties in the range of 10^{-18} (Delva et al., 2019; Lisdat et al., 2016; Mehlstäubler et al., 2018; Grotti et al., 2018). Further ideas propose optical clocks in space, e.g. to establish a homogeneous space reference system (Müller et al., 2018).

In this paper, we use a common-clock setup to investigate the error sources limiting the instability of GNSS links for frequency transfer (FT). In a common-clock experiment, two or more GNSS receivers are supplied with a common reference frequency, resembling the perfect setup for analyzing the impact of errors such as tropospheric delay, since the ground truth is provided by an optical fiber link. The link instability is computed and assessed using different Allan variances depending on the proposed application (D. Allan, 1966; D. W. Allan and Hellwig, 1978; D. W. Allan, 1987). Relative frequency instability of GNSS-based links can reach the range of 10^{-17} over 20–30 days averaging time in terms of modified Allan deviation (MDEV) (Jian et al., 2023; Petit, 2021). We use the same measure of instability in this report. Some studies investigated the performance of GNSS links in comparison with optical clocks and fiber links over long baselines (Droste et al., 2015).

A common-clock setup allows the evaluation of the corresponding link without being limited by the instability and uncertainty of the used frequency source. From previous experiments, we observed low instability for zero and short baselines (2–290 m) with typical MDEV values of 10^{-13} at one second and reaching 10^{-17} at one day averaging time, computed in single difference (SD) or precise point positioning (PPP) approaches (Krawinkel et al., 2022; Elmaghraby et al., 2022). These studies included validating simulations and predefined models to understand the physical meaning behind variations of the differential receiver clock time series (Elmaghraby et al., 2023).

To establish GNSS common-clock experiments, a fiber link equipped with an electronically stabilized time and frequency distribution system (ELSTAB) (Krehlik et al., 2016) can be used. The ELSTAB system, commercially available as OSTT-4L from PIKTime Systems (Poznán, Poland) consists of a local and a remote module connected via single-mode optical fiber, specified for up to a 25 dB fiber loss. Propagation delay fluctuations on the fiber are actively compensated using a pair of electronic variable delay lines on a chip (Śliwczyński et al., 2011). The system distributes a 10 MHz radio frequency and a 1-PPS timing signal via 73 km of single-mode optical fiber between Physikalisch-Technische Bundesanstalt (PTB) and the Hannover Institute of Technology (HITec) at Leibniz University Hannover (LUH), with an instability specified as $3 \cdot 10^{-17}$ MDEV at 10^5 s averaging time.

Extending the separation of the GNSS receivers to several ten kilometers, we challenged our algorithms and performed a common-clock experiment between the building of the HITec at LUH, and the Meitner building at PTB from September 1 until October 9 in 2023 (days of year 244–282). We used the data from the long baseline (Meitner-HITec) to estimate the receiver clock difference between the stations and to investigate the variations caused by the various error sources at both locations. The zero and short baselines provide information about the deviations occurring due to different receiver manufacturers and/or cables, allowing us to eventually eliminate such systematic errors.

In this contribution, we direct our investigation to a one-week data set from the long baseline (Meitner-HITec) so that we get a preliminary idea about link instability and the reliability of the ELSTAB system for the reference transfer via optical fiber. A symmetric setup consisting of GNSS equipment from the same manufacturers was installed at each building. Two Leica AR20 antennas were mounted at each location, each connected to a Septentrio PolaRx5TR receiver, thus forming a local short baseline. In addition, a JAVAD OMEGA receiver was connected to one of those antennas, creating a zero-baseline configuration at that antenna. All of the six receivers were fed with the same 10 MHz frequency signal, generated at PTB by one of the active hydrogen masers (AHMs) located at Kopfermann building, from where the 10 MHz reference signal is transferred via underground coaxial cable to the Paschen building, where it feeds the local modules of two ELSTAB systems. The ELSTAB modules convert the signal to the optical domain and transfer it via optical fiber, where the corresponding ELSTAB remote modules convert it back to an electrical signal given to the receivers. Since the link loss between PTB and HITec exceeds the specifications of the ELSTAB system, a single-path bidirectional optical amplifier was added at an intermediate location at LUH.

We computed single difference common view (SD-CV) of carrier phase observations between the two receivers at the baseline end points, and PPP solutions for estimating the relative receiver clock errors on the long baseline. We extend the SD-CV algorithm with an ambiguity resolution based on wide-lane/narrow-lane ambiguity fixing.

II. Common clock experiment

The common clock experiment was set up between the HITec building at LUH and the Meitner building at PTB. The buildings are separated by approximately 52 km. The experiment took place for more than five weeks from September 1 until October 9 in 2023. A symmetric setup consisting of GNSS equipment from the same manufacturers was installed at each building. Two Leica AR20 antennas were mounted at each location for crosschecking, each connected to a Septentrio PolaRx5TR receiver and thus forming a local short baseline. In addition, a JAVAD OMEGA receiver was connected to one of the antennas, thus creating a zero-baseline configuration at that antenna. The full details of each equipment are listed in table II.

Figure 1 illustrates the installation of four antennas. Two are at the top of Meitner building at PTB, Braunschweig with almost no vertical height differences. The other two antennas were located at HITec building, where the difference in height is around 14 meters. Station coordinates are given in the International Terrestrial Reference Frame ITRF2020 (Altamimi et al., 2023) and used throughout the analysis as fixed reference values and prior information for station coordinates (see table I). All of the six used receivers were fed with the same 10 MHz frequency signal, generated at PTB by one of the AHMs located at Kopfermann building. From there, the 10 MHz reference signal is transferred via underground coaxial cable to the Paschen building, where it feeds the local modules of two ELSTAB systems. The ELSTAB modules convert the electronic 10 MHz signal to the optical domain and transfer it via optical fiber to the Meitner building at PTB and HITec building at LUH in Hannover, where the corresponding ELSTAB remote modules convert it back to an electrical signal given to the three GNSS receivers located at HITec, cf. figure 2.

TABLE I: GNSS stations reference coordinates (ITRF2020)

Station	X [m]	Y [m]	Z [m]
EE01	3845020.94	658102.71	5029365.15
HM01	3845030.72	658092.67	5029341.20
MEI1	3843994.28	709947.16	5023159.75
MEI2	3843994.98	709945.31	5023159.48

III. Data analysis

A. Preprocessing of GNSS data

We focus in the analysis on GPS and Galileo carrier phase and code observations. For GPS, we use the signals on two frequencies L1(C/A) and L2W and for Galileo the observations transmitted on signals E1 and E5a are investigated. Through data pre-processing, we apply a-priori models to correct for the effects influencing the GNSS signals received from the satellites. These models are necessary for precise applications such as time and frequency transfer in particular when PPP algorithms are applied. We use final satellite orbit and clock products from the Center of Orbit Determination in Europe (CODE) (Prange et al., 2020). In addition, the tropospheric delay is assessed using the Global Pressure and Temperature 3 (GPT3) model and the Vienna Mapping Function 3 (VMF3) (Landskron and Böhm, 2018). Carrier phase observations are corrected for the phase wind-up effect as well as phase center offsets and variations derived from the correction data provided by the IGS20 model (Wu et al., 1993; Beyerle, 2009). The code observations are corrected for satellite observable-specific biases (OSBs), also made available by CODE to be consistent with the satellite orbit and clock products. Furthermore, various tidal and loading effects are accounted for according to the IERS 2010 conventions (Petit and Luzum, 2010). As a result, the corrected observations, also named observed- minus- computed values, are obtained. Table III lists for each algorithm the main configurations chosen before the core computations.

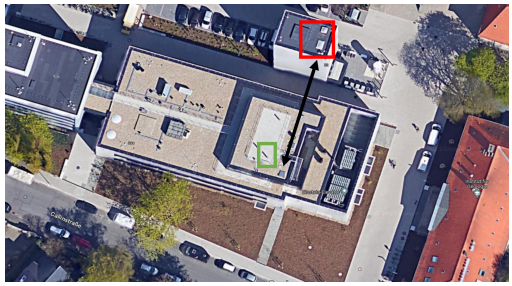

(a) HITec: EE01 antenna (red), HM01 antenna (green)

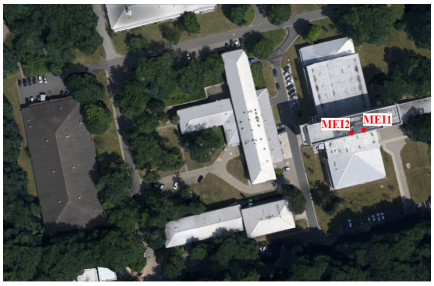

(b) PTB

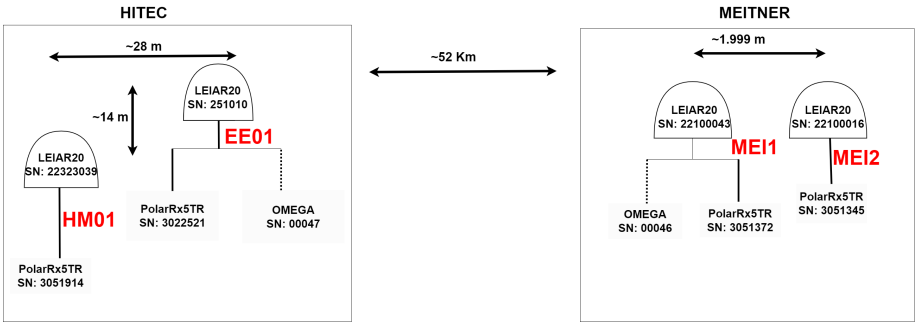

(c) GNSS stations installations at HITec, Hannover and PTB, Braunschweig

Fig. 1: GNSS setup for the common clock experiment (Map data: Google, GeoBasis-DE/BKG)

TABLE II: GNSS equipment

Receiver, SN	Location (initials)	Antenna, SN
Septentrio PolaRx5TR, 3051345	PTB (MEI2)	LEIAR20, 22100043
Septentrio PolaRx5TR, 3051372	PTB (MEI1)	LEIAR20, 22100016
Septentrio PolaRx5TR, 3051914	HITec (HM01)	LEIAR20, 22323039
Septentrio PolaRx5TR, 3022521	HITec (EE01)	LEIAR20, 20251010
Javad OMEGA, 00047	HITec (EE01)	LEIAR20, 20251010
Javad OMEGA, 00046	PTB (MEI1)	LEIAR20, 22100016

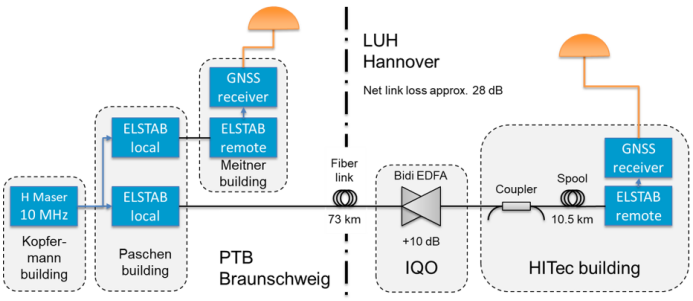

Fig. 2: Optical fiber and ELSTAB system installation

TABLE III: Algorithms main configurations

Parameter	SD-CV	PPP
Elevation cut-off angle	15°	5°
Signal to noise cut-off ratio (C/N_0)	20 dB-Hz	20 dB-Hz
Minimum satellite arc length to include	300 s	1800 s
Weighting function	Identity	$\sqrt{\sin(\text{elevation angle})}$

B. Single difference common view

Differencing carrier phase measurements between receivers is implemented to eliminate the major errors similarly affecting the satellite signals used commonly at our stations. After the main pre-processing step on raw data as shown above, an elevation cut-off is applied as depicted in table III in the case of (SD-CV). Measurements acquired at each station are pre-processed separately. Also, the ionosphere-free (IF) and Melbourne-Wübbena (MW) linear combinations (LCs) (G, 1985; W, 1985) are computed as indicated in equations (1) and (2), respectively.

$$\text{MW} = \frac{f_1}{f_1 - f_2} L_1 - \frac{f_2}{f_1 - f_2} L_2 - \frac{f_1}{f_1 + f_2} P_1 + \frac{f_2}{f_1 + f_2} P_2 \tag{1}$$

$$\text{IF} = \frac{f_1^2}{f_1^2 - f_2^2} L_1 - \frac{f_2^2}{f_1^2 - f_2^2} L_2 \tag{2}$$

where P, L and f represent the code observations, carrier phase observations and signal frequency, respectively. The subscripts 1 and 2 indicate the frequency.

At the respective baseline, we form IF SDs and MW SDs. For simplicity, we refer to both as only IF and MW in the following algorithm steps in this sub-section. Here, Δ specifies the SD parameters between the stations and in equations (3), (5), and A, B refer to first and second station, respectively.

The algorithm to estimate the differential receiver clock error between both stations is performed in the following steps:

1) Estimate the float wide-lane (WL) ambiguities $\Delta\hat{N}_{\mathrm{WL}}$ from the SD MW LC.
2) Fix each WL ambiguity to an integer value, and determine a constant WL receiver bias.
3) Introduce the fixed WL ambiguities $\Delta\check{N}_{\mathrm{WL}}$ into the IF LC and estimate a float narrow-lane (NL) ambiguity together with the tropospheric parameter. The latter is parameterized as a piece-wise linear function with constraints between the segments on the slope.
4) Fix each NL ambiguity to an integer value, and determine a constant NL receiver bias.
5) Correct the tropospheric parameter and compute the final observable.

As shown in equation (3), MW consists of a bias and the WL ambiguity. We estimate the float WL ambiguity $\hat{N}_{\mathrm{WL}}$ from the MW, then the WL ambiguity is fixed by rounding to the nearest integer. Bias b_{MW} is being estimated after fixing the ambiguities by rounding to include the uncalibrated biases between the receivers. This is done by computing the mean value of the fractional part of the estimated WL ambiguity $\hat{N}_{\mathrm{WL}}$.

$$\mathrm{MW}_{AB} = \Delta b_{\mathrm{MW}} + \lambda_{\mathrm{WL}} \cdot \Delta N_{\mathrm{WL}} \tag{3}$$

$$\Delta N_{\mathrm{WL}} = \Delta N_1 - \Delta N_2 \tag{4}$$

As the biases between the satellites should be eliminated after performing the receiver SDs. Receivers' uncalibrated bias is found to be non-zero and stable over the whole period of analyzed data. The fixed WL ambiguities are introduced further to update the IF-LC as formulated in equation (5), where $\Delta\tau$ is the receiver clock difference, our parameter of interest, Δb_{IF} the differential receiver bias when forming IF between two frequencies, ΔT the relative tropospheric delay, ΔN_1 the differential float ambiguity of the first frequency, and λ_N the narrow lane ambiguity of ca. $10.4\,\mathrm{cm}$.

$$\mathrm{IF}_{AB} = c \cdot \Delta\tau + \Delta b_{\mathrm{IF}} + \Delta T + \lambda_N \cdot \left(\Delta N_1 + \frac{\lambda_{\mathrm{WL}}}{\lambda_2} \cdot \Delta\check{N}_{\mathrm{WL}} \right) \tag{5}$$

After subtracting the constant part of the fixed WL ambiguity, the IF reads:

$$\mathrm{IF}_{\mathrm{WL,fixed}} = c \cdot \Delta\tau + \Delta b_{\mathrm{IF}} + \Delta T + \lambda_N \cdot \Delta N_1 \tag{6}$$

It is possible to estimate the other parameters; the least-squares adjustment has been divided into two parts to eliminate the rank deficiency of the system. The tropospheric delay decorrelates temporally with the receiver clock, while ambiguities and bias remain constant over each satellite arc or for all observation, respectively. Thus, we solve the system to acquire the estimates of the relative tropospheric delay and float ambiguities. The latter is estimated for each available arc for each day, and the first is estimated in one-hour segments over 24 hours. Each segment is modeled as a piece-wise linear fit, where the offset and slope are constrained with adjustable characteristic translated mathematically in the standard deviation vector used in the least-squares adjustment. This vector is depicted in equation (7):

$$\sigma_{\mathrm{constraints}} = \begin{bmatrix} \sigma_{\mathrm{offset}} & \sigma_{\mathrm{slope}} \end{bmatrix} = \begin{bmatrix} 10^{-4}\,\mathrm{m} & 8 \cdot 10^{-3}\,\mathrm{m/segment} \end{bmatrix} \tag{7}$$

The full matrix system with H, y and V being the design matrix, observations vector and variance matrix, respectively, reads as followed:

$$H = \begin{bmatrix} H_{\mathrm{troposphere}} & H_{\mathrm{ambiguities}} \\ C_{\mathrm{offset+slope}} & 0 \end{bmatrix} \tag{8}$$

$$y = \begin{bmatrix} y_{\mathrm{observations}} \\ y_{\mathrm{constraints}} \end{bmatrix} \tag{9}$$

$$V = \begin{bmatrix} \sigma^2_{\mathrm{observations}} & 0 \\ 0 & \sigma^2_{\mathrm{constraints}} \end{bmatrix} \tag{10}$$

The LAMBDA method is used to fix the float ambiguities $\hat{N}_1$, where integer search estimator is applied (Teunissen, 1990; Peter J. G. Teunissen, 1995). The fixed ambiguities $\check{N}_1$, and their variance-covariance matrices, are used afterwards to compute the tropospheric fixed solution as shown by equation (11). Then we apply both parameters correcting the IF WL fixed solution to compute the IF final fixed solution by compensating the offsets between the computed relative tropospheric segments to estimate the receiver clock differences as mentioned in equation (12):

$$\Delta\check{T} = \Delta\hat{T} - Q_{\Delta\hat{T}\,\Delta\hat{N}_1} \cdot Q^{-1}_{\Delta\hat{N}_1} \left(\hat{N}_1 - \check{N}_1 \right) \tag{11}$$

Finally, the differential receiver clock error can be obtained from:

$$\mathrm{IF}_{\mathrm{WL\text{-}NL,fixed}} = \Delta b_{\mathrm{IF}} + \Delta\tau \tag{12}$$

C. Precise point positioning

Each station involved in a PPP solution is processed independently. We first analyze GPS and Galileo data with the PPP module of our in-house developed MATLAB-based software, which consists of a linearized Kalman filter with a fixed-interval forward-backward smoother (Gelb et al., 1974). We use a filter update interval of 30 seconds and an elevation-dependent observation weighting scheme where the weight p_i of the i-the observation is determined by the relation

$$p_i = 1/\sqrt{\sin(E_i)} \tag{13}$$

with elevation angle E. Due to the relatively low elevation cutoff angle of 5°, we also estimate horizontal gradients in addition to the zenith path delays as tropospheric parameters (Chen and Herring, 1997). Further filter states are the receiver coordinates, the receiver clock error as well as float carrier phase ambiguities. The coordinates, horizontal gradients and the ambiguities are each modeled as random constant processes. The zenith path delay follows a random walk process with a spectral amplitude of $(0.003\,\mathrm{m})^2$/hour. The clock error is represented by a random ramp process according to the model of (van Dierendonck et al., 1984; Krawinkel and Schön, 2016) using the spectral coefficients of a temperature compensated crystal oscillator (TCXO) (Brown and Hwang, 2012).

D. Optical fiber data

Prior to deployment, the performance of the ELSTAB system was confirmed on a lab-based physical model of the link (Link-Sim), allowing for a direct comparison of the transmitted signal with the reference and the error signal generated by the ELSTAB stabilization system. Upon deployment on the link, performance was then monitored by observing reference and error signal only. While this "in-loop" signal does not, stritcly speaking, allow us to characterize the instability of the transmitted reference at HITec, comparing it with the data from the physical model allows us to determine that the system is working properly, and hence can be expected to perform to specification and similarly to the physical model "out-of-loop" measurement. Frequency data was recorded using a K+K frequency counter with FHR module (by K+K Messtechnik GmbH, Braunschweig, Germany), and recorded data was subsequently processed as described in (Riley, 2008) and the MDEV plotted using Allan Tools (2019.7) in Python (3.10.13).

IV. Results and discussion

We discuss here the results of the algorithms developed at our institute, namely PPP and SD-CV. The chosen baselines are those between HITec building in Hannover and Meitner building at PTB in Braunschweig. For this distance, there are four receivers selected to create two differential receiver clock time series as explained before in section III.

Figures 3 and 4 present the results from the SD-CV algorithm for GPS and Galileo, respectively. Time series of both show variations in peak-to-peak range of ± 40 mm, with maximum values on day one (September 12, 2023), and are almost zero mean. The differences between the time series are due to local effects at the different antenna locations. Effects common to both time series are related to remaining atmospheric influences as well as the way of data processing and potential deficiencies which will be improved in a future version of our algorithm. One example of these effects is the high oscillation on day one: shortening the processing segments for the troposphere from one hour to 15 minutes significantly reduces the observed variations.

The PPP results for the corresponding baselines are depicted in figures 5 for GPS and 6 for Galileo, respectively. Other than SD-CV, the time series from PPP still experience day boundary discontinuities impacting the GNSS-based frequency instability. As can be seen in figures 4 and 6, variations are similar between SD-CV and PPP solutions for Galileo especially for the baseline variant EE01-MEI1.

The MDEV is computed for both algorithms. Figure 7 summarizes the computed instability for all baselines. We distinguish lower instability from PPP solution over short averaging periods with approximately $1.5{\cdot}10^{-13}$ while SD-CV achieves ca. $3{\cdot}10^{-13}$ at 30 seconds. This may be due to fewer GNSS satellites contributing to the SD-CV solution due to the applied large cut-off angle and the different weighting scheme. SD-CV achieves lower instability values between $3{\cdot}10^{-17}$ and $1{\cdot}10^{-16}$, and PPP is almost one order of magnitude higher with values between $2{\cdot}10^{-16}$ and $1{\cdot}10^{-15}$ at one-day averaging. At an averaging time of one hour, a small bump is visible which can be attributed to the tropospheric modeling, since when using shorter segments for the piece-wise linear modeling, the bump is reduced and shifted towards shorter averaging times. It is noted that the MDEV of the PPP solution is hitting the noise floor at ca. $6 \cdot 10^{-16}$ for baseline HM01-MEI2 as shown in figure 7. It also shows random walk behavior, which can be visually identified from the time series of clock differences in figure 5b.

In figure 8, MDEV is plotted for one baseline EE01-MEI1 instability of our two main links in this experiment. In addition, the "in-loop" MDEV of the 10 MHz signal distributed by ELSTAB as reference on the fiber link between Braunschweig and Hannover (dashed, yellow) and the "out-of-loop" MDEV of ELSTAB compared to its own reference in the lab-based physical model of the link (Link-Sim; dot-dashed, blue) are given, confirming that for averaging times shorter than 10^5 s, ELSTAB via optical fiber outperforms the satellite connections, as required for this experiment. In addition, the performance of the ELSTAB system was previously assessed in field experiments. In (Sliwczynski et al., 2020) a reference signal was compared against its copy which passed through a chain of three optical fiber links from PTB in Braunschweig to Bremen and back to Braunschweig via a different route through Hannover. Three sets of terminals were concatenated and four in-line bidirectional optical amplifiers were involved. The total length of the fibers was about 450 km. The measured instability of that much longer link was below all respective GNSS instability data of this work, which are depicted in figures 7 and 8. Additional published assessments of field-deployed ELSTAB can be found in (Krehlik et al., 2016; Śliwczyński et al., 2017). In these tests, a 10 MHz reference signal was compared with a copy which was passed through one or more ELSTAB systems (out-of-loop test). The measured instabilities were also at least an order of magnitude below GNSS instability data of this work for averaging times up to 10^4 s, and comparable to SD-CV GNSS data at 10^5 s.

V. Conclusions

In our study, we performed a common-clock experiment for a 52 km baseline, where a stabilized frequency signal is transmitted through an optical fiber by using ELSTAB systems. This configuration is a valid experiment to test and improve the instability of GNSS frequency transfer. We analyzed our PPP algorithm and proposed a new SD-CV algorithm for GNSS FT. Computing linear combinations, the carrier phase ambiguities could be fixed and instabilities in the range of $1\text{–}3 \cdot 10^{-17}$ at one day averaging time could be achieved. Which is almost one order of magnitude better than the result obtained from PPP. Furthermore, the ELSTAB as a conversion system used for long baselines optical fiber is sufficient for serving as ground-truth for GNSS FT in common clock set-ups. Next steps will be directed to improve the SD-CV algorithm in terms of modeling the tropospheric refraction and selection of observation weighting.

Acknowledgment

This research was funded by the Deutsche Forschungsgemeinschaft (DFG, German Research Foundation) – project

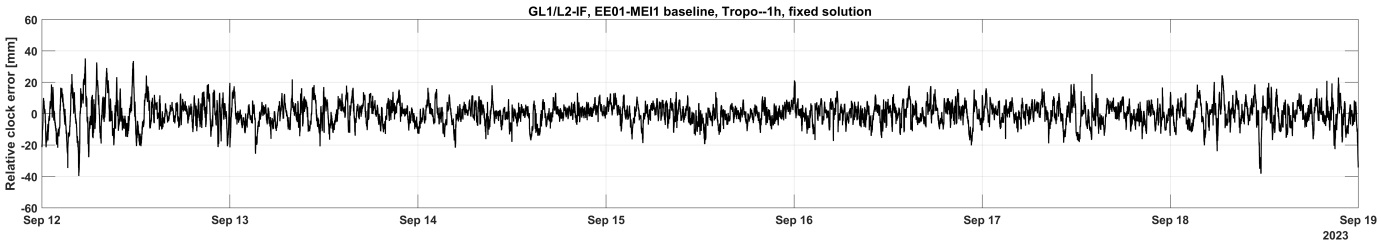

(a) EE01-MEI1

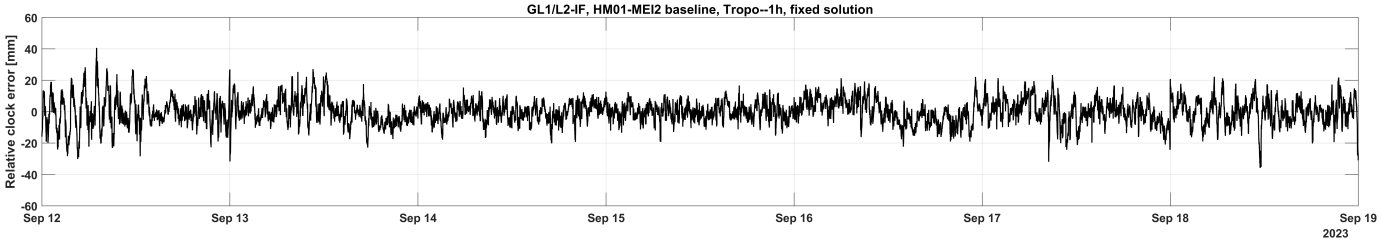

(b) HM01-MEI2

Fig. 3: Estimated receiver clock difference using SD-CV algorithm at signals GPS L1(C/A) and L2W

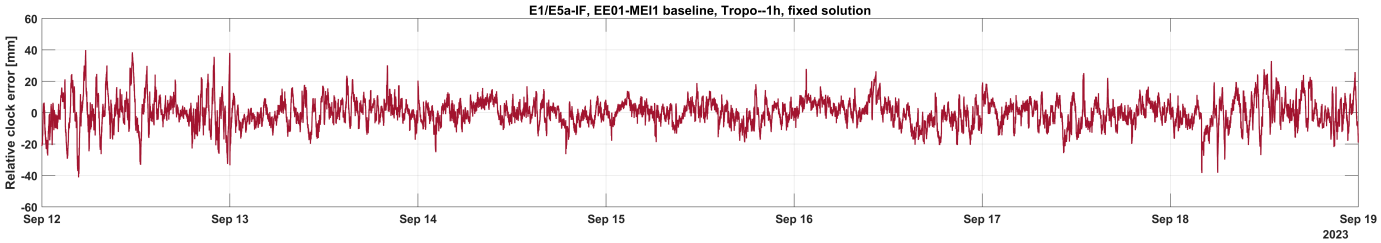

(a) EE01-MEI1

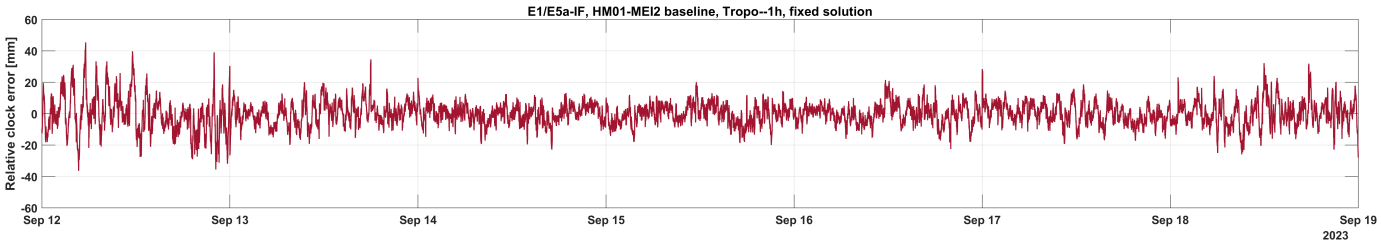

(b) HM01-MEI2

Fig. 4: Estimated receiver clock difference using SD-CV algorithm at signals Galileo E1 and E5a

number 434617780 – SFB 1464, and by the German Federal Ministry of Education and Research (BMBF) within the collaborative project QR.X (16KISQ017). A part of the GNSS equipment used was funded under DFG INST 187/774-1 FUGG.

DISCLAIMER

The authors do not attempt to recommend any of the instruments under test. It is noted that the performance of the equipment presented in this contribution depends on the particular environment and the individual instruments in use. Other instruments of the same type or the same manufacturer may show different behavior. The readers are, however, encouraged to test their own equipment to identify the system performance with respect to a particular application.

REFERENCES

Allan, D. (1966). “Statistics of atomic frequency standards”. In: *Proceedings of the IEEE* 54.2, pp. 221–230. DOI: 10.1109/PROC.1966.4634.

Allan, D. W. (1987). “Time and Frequency (Time-Domain) Characterization, Estimation, and Prediction of Precision Clocks and Oscillators”. In: *IEEE Transactions on Ultrasonics, Ferroelectrics and Frequency Control* 34.6, pp. 647–654.

Allan, D. W. and H. Hellwig (1978). “Time Deviation and Time Prediction Error for Clock Specification, Characterization, and Application”. In: *Proceedings of the IEEE Position, Location and Navigation Symposium*. San Diego, USA, pp. 22–28.

Altamimi, Z., P. Rebischung, X. Collilieux, L. Métivier, and K. Chanard (2023). “ITRF2020: an augmented reference

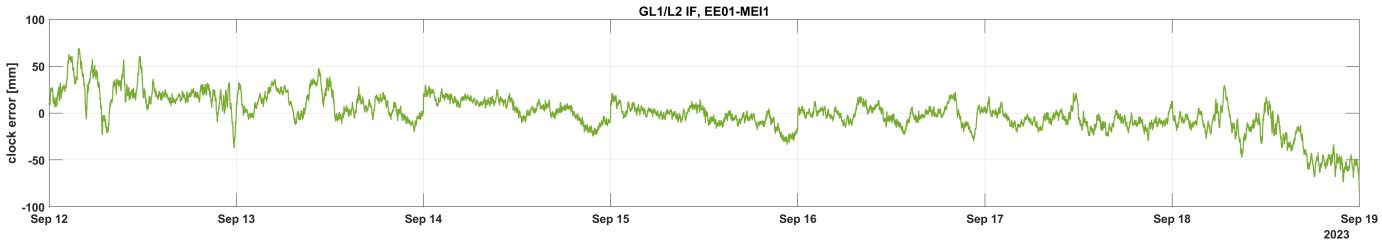

(a) EE01-MEI1

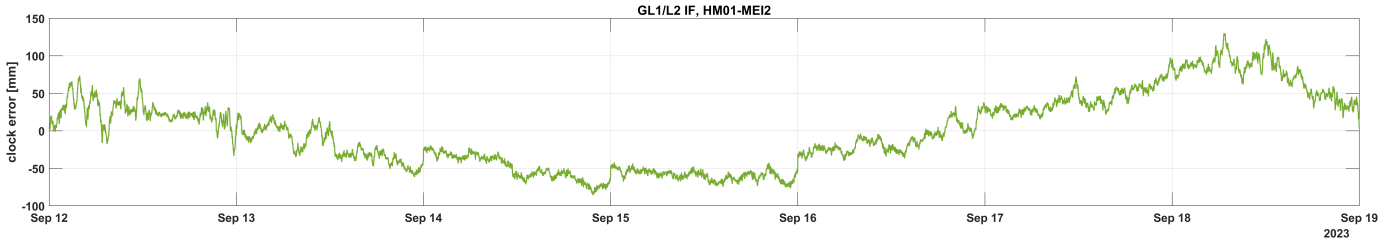

(b) HM01-MEI2

Fig. 5: Estimated receiver clock difference using PPP algorithm at signals GPS L1(C/A) and L2W

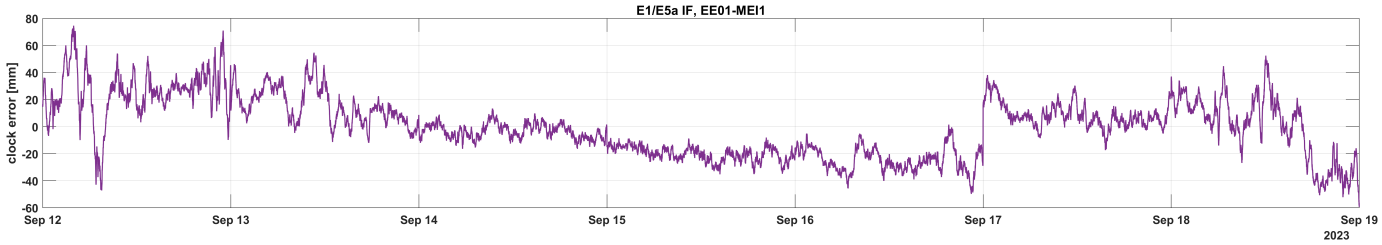

(a) EE01-MEI1

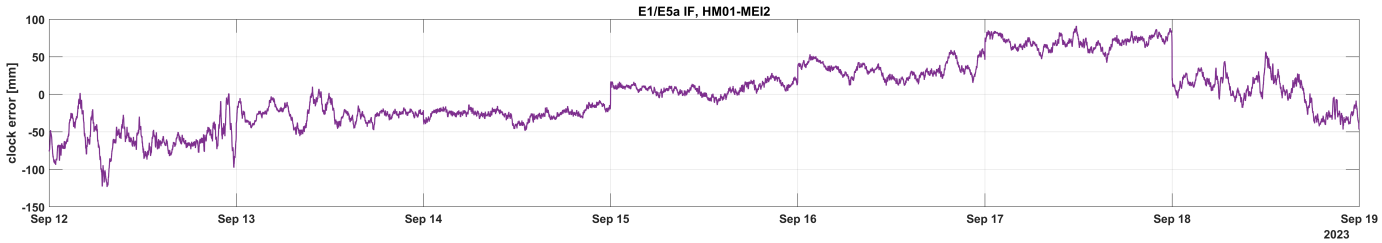

(b) HM01-MEI2

Fig. 6: Estimated receiver clock difference using PPP algorithm at signals Galileo E1 and E5a

frame refining the modeling of nonlinear station motions". In: *Journal of Geodesy* 97.5, pp. 1–22. DOI: 10.1007/s00190-023-01738-w. URL: https://link.springer.com/article/10.1007/s00190-023-01738-w.

Bauch, A., D. Piester, T. Polewka, and E. Staliuniene (2020). "On the possibility of getting traceable time and frequency measurements via GNSS receivers". In: *GPS Solutions* 24.4, pp. 1–13. DOI: 10.1007/s10291-020-01024-8. URL: https://link.springer.com/article/10.1007/s10291-020-01024-8.

Beyerle, G. (2009). "Carrier phase wind-up in GPS reflectometry". In: *GPS Solutions* 13.3, pp. 191–198. DOI: 10.1007/s10291-008-0112-1.

Brown, R. G. and P. Y. C. Hwang (2012). *Introduction to Random Signals and Applied Kalman Filtering*. 4th edition. John Wiley & Sons.

Chen, G. and T. A. Herring (1997). "Effects of atmospheric azimuthal asymmetry on the analysis of space geodetic data". In: *Journal of Geophysical Research: Solid Earth* 102.B9, pp. 20489–20502. DOI: 10.1029/97JB01739.

Defraigne, P., J. Achkar, M. J. Coleman, M. Gertsvolf, R. Ichikawa, J. Levine, P. Uhrich, P. Whibberley, M. Wouters, and A. Bauch (2022). "Achieving traceability to UTC through GNSS measurements". In: *Metrologia* 59.6, p. 064001. DOI: 10.1088/1681-7575/ac98cb. URL: https://iopscience.iop.org/article/10.1088/1681-7575/ac98cb.

Defraigne, P., E. Pinat, G. Petit, and F. Meynadier (2023). "Monitoring of the offset between UTC and its prediction broadcast by the GNSS". In: *Metrologia* 60.6, p. 065010. DOI: 10.1088/1681-7575/ad0562. URL: https://iopscience.iop.org/article/10.1088/1681-7575/ad0562#metad0562s6.

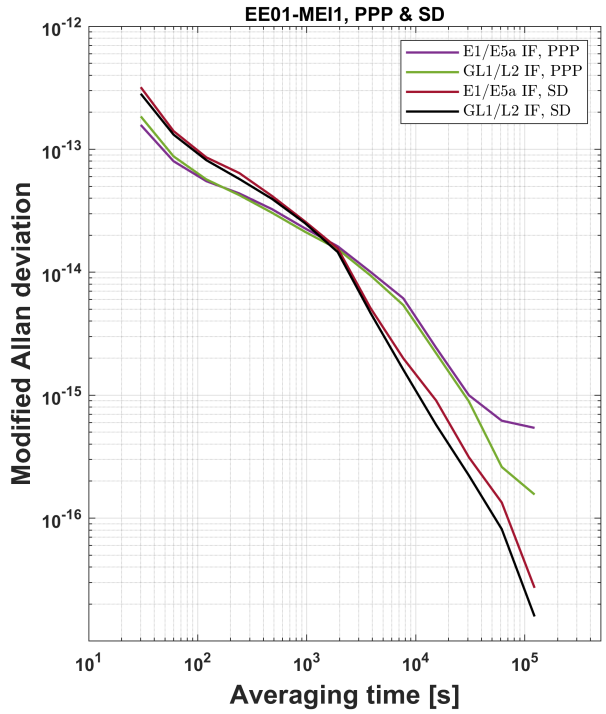

(a) EE01-MEI1

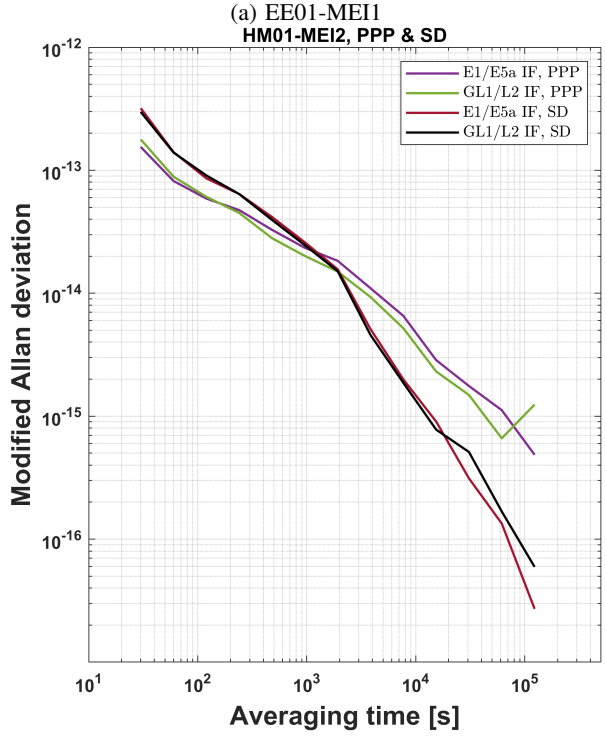

(b) HM01-MEI2

Fig. 7: Modified Allan deviation of PPP and SD-CV for GPS and Galileo

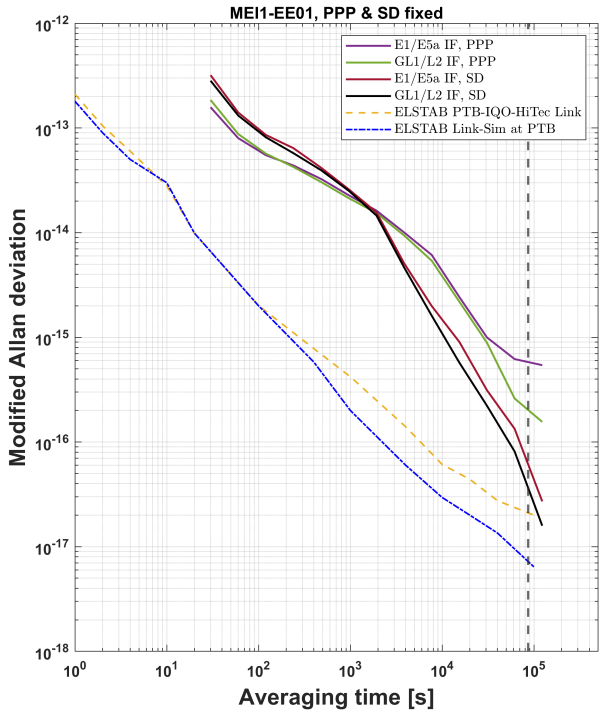

Fig. 8: Modified Allan deviation of PPP and SD-CV for GPS and Galileo, and the estimated instability of optical fiber and ELSTAB system

Defraigne, P. (2017). "GNSS Time and Frequency Transfer". In: *Springer Handbook of Global Navigation Satellite Systems*. Ed. by P. J. G. Teunissen and O. Montenbruck. Springer International Publishing, pp. 1187–1206. DOI: 10.1007/978-3-319-42928-1{\textunderscore}33.

Delva, P., H. Denker, and G. Lion (2019). "Chronometric Geodesy: Methods and Applications". In: *Relativistic Geodesy: Foundations and Applications*. Ed. by D. Puetzfeld and C. Lämmerzahl. Cham: Springer International Publishing, pp. 25–85. DOI: 10.1007/978-3-030-11500-5_2. URL: https://doi.org/10.1007/978-3-030-11500-5_2.

Droste, S., C. Grebing, J. Leute, S. Raupach, A. Matveev, T. Hänsch, A. Bauch, R. Holzwarth, and G. Grosche (2015). "Characterization of a 450 km baseline GPS carrier-phase link using an optical fiber link". In: *New Journal of Physics* 17.8. DOI: 10.1088/1367-2630/17/8/083044.

Elmaghraby, A., T. Krawinkel, and S. Schön (2022). "Inventory of Error Sources Limiting GNSS-based Frequency Transfer". In: *2022 Joint Conference of the European Frequency and Time Forum and IEEE International Frequency Control Symposium (EFTF/IFCS)*, pp. 1–9. DOI: 10.1109/EFTF/IFCS54560.2022.9850608.

Elmaghraby, A., T. Krawinkel, S. Schön, D. Piester, and A. Bauch (2023). "On Error Modeling in GNSS-based Frequency Transfer: Effects of Temperature Variations and Satellite Orbit Repeat Times". In: *Proceedings of the 54th Annual Precise Time and Time Interval Systems and Applications Meeting*. The Precise Time and Time Interval Systems and Applications Meeting. Institute of Navigation, pp. 23–37. DOI: 10.33012/2023.18699.

G, W. (1985). "Software developments for geodetic positioning with GPS using TI-4100 code and carrier measurements". In: *Proceedings 1st international symposium on precise positioning with the global positioning system. Rockville, Maryland, USA*, pp. 403–412.

Gelb, A., J. F. Kasper, R. A. Nash, C. F. Price, and A. A. Sutherland (1974). *Applied Optimal Estimation*. Ed. by A. Gelb. The M.I.T. Press.

Grotti, J., S. Koller, S. Vogt, S. Häfner, U. Sterr, C. Lisdat, H. Denker, C. Voigt, L. Timmen, A. Rolland, F. N. Baynes, H. S. Margolis, M. Zampaolo, P. Thoumany, M. Pizzocaro, B. Rauf, F. Bregolin, A. Tampellini, P. Barbieri, M. Zucco, G. A. Costanzo, C. Clivati, F. Levi, and D. Calonico (2018). *Geodesy and metrology with a transportable optical clock*. DOI: 10.1038/s41567-017-0042-3. URL: https://arxiv.org/pdf/1705.04089.

Jian, B., S. Beattie, S. Weyers, J. Rahm, B. Donahue, and M. Gertsvolf (2023). "GPS PPP-AR frequency transfer and its application for comparing atomic fountain primary frequency standards between NRC and PTB". In: *Metrologia* 60.6, p. 065002. DOI: 10.1088/1681-7575/acfa04. URL: https://iopscience.iop.org/article/10.1088/1681-7575/acfa04.

Krawinkel, T., A. Elmaghraby, and S. Schön (2022). "Exploring the Technical Limits of GNSS-based Frequency Transfer". In: *Proceedings of the 53rd Annual Precise Time and Time Interval Systems and Applications Meeting*. The Precise Time and Time Interval Systems and Applications Meeting. Institute of Navigation, pp. 188–198. DOI: 10.33012/2022.18288.

Krawinkel, T. and S. Schön (2016). "Benefits of receiver clock modeling in code-based GNSS navigation". In: *GPS Solutions* 20 (4), pp. 687–701. DOI: 10.1007/s10291-015-0480-2.

Krehlik, P., L. Śliwczynski, L. Buczek, J. Kolodziej, and M. Lipinski (2016). "ELSTAB—Fiber-Optic Time and Frequency Distribution Technology: A General Characterization and Fundamental Limits". In: *IEEE Transactions on Ultrasonics, Ferroelectrics, and Frequency Control* 63.7, pp. 993–1004. DOI: 10.1109/TUFFC.2015.2502547.

Landskron, D. and J. Böhm (2018). "VMF3/GPT3: refined discrete and empirical troposphere mapping functions". In: *Journal of Geodesy* 92 (4), pp. 349–360. DOI: 10.1007/s00190-017-1066-2.

Lisdat, C., G. Grosche, N. Quintin, C. Shi, S. M. F. Raupach, C. Grebing, D. Nicolodi, F. Stefani, A. Al-Masoudi, S. Dörscher, S. Häfner, J.-L. Robyr, N. Chiodo, S. Bilicki, E. Bookjans, A. Koczwara, S. Koke, A. Kuhl, F. Wiotte, F. Meynadier, E. Camisard, M. Abgrall, M. Lours, T. Legero, H. Schnatz, U. Sterr, H. Denker, C. Chardonnet, Y. Le Coq, G. Santarelli, A. Amy-Klein, R. Le Targat, J. Lodewyck, O. Lopez, and P.-E. Pottie (2016). "A clock network for geodesy and fundamental science". In: *Nature Communications* 7.1, p. 12443. DOI: 10.1038/ncomms12443. URL: https://www.nature.com/articles/ncomms12443.

Mehlstäubler, T. E., G. Grosche, C. Lisdat, P. O. Schmidt, and H. Denker (2018). "Atomic clocks for geodesy". In: *Reports on progress in physics. Physical Society (Great Britain)* 81.6, p. 064401. DOI: 10.1088/1361-6633/aab409.

Müller, J., D. Dirkx, S. M. Kopeikin, G. Lion, I. Panet, G. Petit, and Visser, P. N. A. M. (2018). "High Performance Clocks and Gravity Field Determination". In: *Space Science Reviews* 214.1, pp. 1–31. DOI: 10.1007/s11214-017-0431-z. URL: https://link.springer.com/article/10.1007/s11214-017-0431-z.

Peter J. G. Teunissen (1995). "The least-squares ambiguity decorrelation adjustment: a method for fast GPS integer ambiguity estimation". In: *Journal of Geodesy* 70.1-2, pp. 65–82. DOI: 10.1007/BF00863419. URL: https://link.springer.com/article/10.1007/BF00863419.

Petit, G. (2021). "Sub-10^{-16} accuracy GNSS frequency transfer with IPPP". In: *GPS Solutions* 25.1. DOI: 10.1007/s10291-020-01062-2.

Petit, G. and B. Luzum, eds. (2010). *IERS Conventions (2010)*. Vol. 36. IERS Technical Note. Frankfurt am Main: Verlag des Bundesamts für Kartographie und Geodäsie and Verl. des Bundesamts für Kartographie und Geodäsie.

Piester, D., E. Staliuniene, and A. Bauch (2024). "Traceable frequency measurements with counters". In: *Measurement Science and Technology* 35.4, p. 045012. DOI: 10.1088/1361-6501/ad1c4a. URL: https://iopscience.iop.org/article/10.1088/1361-6501/ad1c4a.

Prange, L., A. Villiger, D. Sidorov, S. Schaer, G. Beutler, R. Dach, and A. Jäggi (2020). "Overview of CODE's MGEX solution with the focus on Galileo". In: *Advances in Space Research* 66.12, pp. 2786–2798. DOI: 10.1016/j.asr.2020.04.038.

Riley, W. J. (2008). *Handbook of frequency stability analysis*. Gaithersburg, MD. DOI: 10.6028/NIST.SP.1065.

Sliwczynski, L., P. Krehlik, H. Imlau, H. Ender, H. Schnatz, D. Piester, and A. Bauch (2020). "Fiber-Based UTC Dissemination Supporting 5G Telecommunications Networks". In: *IEEE Communications Magazine* 58.4, pp. 67–73. DOI: 10.1109/MCOM.001.1900599.

Śliwczyński, L., P. Krehlik, L. Buczek, and M. Lipiński (2011). "Active Propagation Delay Stabilization for Fiber-Optic Frequency Distribution Using Controlled Electronic Delay Lines". In: *IEEE Transactions on Instrumentation and Measurement* 60.4, pp. 1480–1488. DOI: 10.1109/TIM.2010.209069.

Śliwczyński, L., P. Krehlik, J. Kołodziej, H. Imlau, H. Ender, H. Schnatz, D. Piester, and A. Bauch (2017). "Fiber-Optic Time Transfer for UTC-Traceable Synchronization for Telecom Networks". In: *IEEE Communications Standards Magazine* 1.1, pp. 66–73. DOI: 10.1109/MCOMSTD.2017.1600766ST.

Teunissen, P. J. G. (1990). "Quality Control in Integrated Navigation Systems". In: *IEEE Aerospace and Electronic Systems Magazine* 5 (7), pp. 35–41. DOI: 10.1109/62.134219.

van Dierendonck, A. J., J. B. McGraw, and R. G. Brown (1984). "Relationship Between Allan Variances and Kalman Filter Parameters". In: *Proceedings of the 16th Annual Precise Time and Time Interval Systems and Applications Meeting*, pp. 273–292.

W, M. (1985). "The case for ranging in GPS based geodetic systems." In: *Proceedings 1st international symposium on precise positioning with the global positioning system. Rockville, Maryland, USA*, pp. 73–386.

Wu, J. T., S. C. Wu, Hajj G. A., W. I. Bertiger, and Lichten S. M. (1993). “Effects of antenna orientation on GPS carrier phase”. In: *Manuscripta Geodaetica* 18.2, pp. 91–98.